CHARACTERIZING STRESS ROUGHNESS AT UTAH FORGE THROUGH SIMULATION OF HYDRAULIC FRACTURE GROWTH DURING 16A STAGE 3 STIMULATION

Organization:	University of Utah
Recipient Organization:	Lawrence Livermore National Laboratory
DUNS Number:	009095365
Recipient Address:	7000 East Ave. Livermore, CA 94550

Award Number:	2-2446
Project Title:	Closing the loop between in situ stress complexity and EGS fracture complexity
Project Period:	10/01/2021 – 06/30/2025

Principal Investigator(s):	Matteo Cusini (PI) cusini1@llnl.gov Andrew Bunger (Co-PI) bunger@pitt.edu
Report prepared by:	Fan Fei (LLNL) Matteo Cusini (LLNL)
Report Submitted by:	Matteo Cusini

Date of Report Submission:	January 30, 2025
Related milestones:	MILESTONE 3.1.1 & 3.2.1

This work was performed under the auspices of the U.S. Department of Energy by Lawrence Livermore National Laboratory under Contract DE-AC52-07NA27344.

1 Introduction

In most geologic formations, the vertical gradient of the minimum horizontal stress (σ_h) exceeds the hydrostatic gradient, often driving hydraulic fractures to propagate upward. However, observations indicate that the upward growth of real hydraulic fractures is less pronounced than theoretical predictions based on smoothly varying σ_h fields. In fact, the layered structure of sedimentary rocks hinders fracture propagation across layers, partially explaining the limited height growth observed in practice (Zoback et al., 2022). While crystalline rocks lack the pervasive layered fabric of sedimentary formations, they still possess structural fabric formed over their geologic history, resulting in inherently "rough" in situ stress fields. Recent studies have identified another key factor: the "roughness" of in situ stress, characterized by temporal, relatively short-wavelength fluctuations superimposed on the overall stress gradient. This stress roughness leads to apparent toughness anisotropy, where the vertical toughness appears significantly larger than the horizontal toughness (P. Fu et al., 2019; Dontsov & Suarez-Rivera, 2021). Neglecting the effects of rock fabric and stress roughness can yield inaccurate predictions of hydraulic fracture geometry and growth rates at larger length scales.

Moderate apparent toughness anisotropy at Utah FORGE was also noted in previous work (McClure, 2023), which modeled hydraulic fractures from Well 16A at the site.The estimated stress gradient at this site is considerably higher than the hydrostatic pressure gradient, which theoretically should result in significant vertical fracture growth. However, microseismic (MEQ) data suggests the fractures are nearly circular. Various explanations for this observation have been proposed, such as natural fractures that inhibit vertical fracture growth. However, it is reasonable to hypothesize that the apparent toughness anisotropy arises from stress roughness within the formation.

This work seeks to explore this hypothesis by comparing the level of toughness anisotropy indicated by the microseismic data to that expected from the stress profile derived from other field measurements. First, we analyze the microseismic data from Utah FORGE to infer the shape and vertical and horizontal growth rates of the hydraulic fractures. Then, we calibrate a numerical hydraulic fracture simulator (i.e., GEOS (Settgast et al., 2024)) to quantify the level of toughness anisotropy required to match the field observations. Finally, we compare this apparent toughness anisotropy to values inferred from stress profiles obtained through sonic logs.

The remainder of this report is organized as follows. Section 2 describes the modeling approach, including the mathematical model, discretization methods, and solution strategies. Section 3 presents an analysis of the MEQ data collected at Utah FORGE, detailing the inferred fracture geometry and propagation rates. Section 4 provides a numerical model of the Stage 3

stimulation performed in 2021, focusing on the calibration of toughness anisotropy to match field observations and a comparison to values derived from well logs. Finally, Section 5 offers conclusions and outlines directions for future work.

2 Numerical model

To model the stimulation activities at Utah FORGE, we employ the hydraulic fracturing module of the GEOS simulation framework (Settgast et al., 2024). The following subsections briefly describe the mathematical formulation,, the discretization method and the solution strategy employed, and the hydraulic fracture propagation criterion.

2.1 Formulation

Here, we define the mathematical model describing the flow of a single phase fluid in a porous domain (Ω) constituting of a (or a system of) fracture (Γ), and a surrounding rock ($\Omega \setminus \Gamma$) along with the mechanical deformation of the domain in the time interval $\mathcal{T} = [0, T_{max}]$. The strong form of the initial-boundary-value problem consists in finding the displacement (u) and the pressure (p) that satisfy the following system of partial differential equations (PDEs)

$$\boldsymbol{\nabla} \cdot \boldsymbol{\sigma} = \mathbf{0} \quad \text{in } \Omega \times \mathcal{T}, \tag{1}$$

$$\frac{\partial}{\partial t}\left(\rho_f \phi\right) + \boldsymbol{\nabla} \cdot \left(\rho_f \boldsymbol{q}_m\right) = q_{ms} \quad \text{in } \Omega\backslash\Gamma \times \mathcal{T} \tag{2}$$

$$\frac{\partial}{\partial t}\left(\rho_f \omega_h\right) + \boldsymbol{\nabla} \cdot \left(\rho_f \omega_h \boldsymbol{q}_f\right) + \boldsymbol{q}_{mf} = \boldsymbol{q}_{fs} \quad \text{in } \Gamma \times \mathcal{T}, \tag{3}$$

$$\boldsymbol{\sigma} \cdot \boldsymbol{n}_{\Gamma+} = -\boldsymbol{\sigma} \cdot \boldsymbol{n}_{\Gamma-} = -p\boldsymbol{n}_{\Gamma+} + \boldsymbol{t}_\Gamma \quad \text{on } \Gamma \times \mathcal{T} \tag{4}$$

$$\tag{5}$$

subject to

$$\boldsymbol{u} = \hat{\boldsymbol{u}} \quad \text{on } \partial_u\Omega, \tag{6}$$

$$\boldsymbol{\sigma} \cdot \boldsymbol{n}_t = \hat{\boldsymbol{t}} \quad \text{on } \partial_t\Omega, \tag{7}$$

$$p = \hat{p}_m \quad \text{on } \partial_p\Omega, \tag{8}$$

$$\boldsymbol{q}_m \cdot \boldsymbol{n}_t = \hat{q}_m \quad \text{on } \partial_q\Omega. \tag{9}$$

Here, Eq. (1) is the linear momentum balance and $\boldsymbol{\sigma}$ is the total Cauchy stress tensor. $\partial_t\Omega$,

$\partial_u\Omega$ are a non-overlapping partition of the exterior boundary of the domain Ω and $\hat{\boldsymbol{t}}$ and $\hat{\boldsymbol{u}}$ denote the prescribed traction and displacement on the exterior boundary, respectively, and $\boldsymbol{n}_t$ is the unit vector normal of $\partial_t\Omega$. Equation (2) describes, instead, the fluid mass balance in the rock matrix. Additionally, $\boldsymbol{q}_m$ is the the fluid velocity in the rock matrix which, according to Darcy's law, reads

$$\boldsymbol{q}_m = -\frac{1}{\mu_f}\boldsymbol{k} \cdot \boldsymbol{\nabla} p_m, \tag{10}$$

where μ_f is the fluid viscosity, $\boldsymbol{k}$ is the permeability tensor and p_m is the fluid pressure in the rock matrix. $\boldsymbol{q}_{ms}$ are the source/sink term in the rock matrix. $\partial_p\Omega$, $\partial_q\Omega$ are another non-overlapping partition of the exterior boundary of Ω $\hat{p}_m$ and $\hat{q}_m$ are the prescribed fluid pressure and fluid velocities.

Equation (3) describes the fluid mass balance in the fractures where ω_h is the hydraulic aperture, $\boldsymbol{q}_{mf}$ is the mass flux between the fracture and the porous medium (leak-off) and $\boldsymbol{q}_f$ is the fluid velocity within the fracture which, according to lubrication theory, can be computed as

$$\boldsymbol{q}_f = -\frac{\omega_h^2}{12\mu_f}\boldsymbol{\nabla} p_f. \tag{11}$$

Here, w_h is the hydraulic aperture of the fracture.

Finally, Equation (4) is the stress continuity constraint across Γ, where $\boldsymbol{t}_\Gamma$ is the contact force. Note that, for an open fracture, the contact force is equal to 0.

2.2 Discretizaiton & solution strategy

Equations (1), (2), and (3) are spatially discretized using a first-order finite element method for the mechanics equations, coupled with a two-point flux approximation-based finite volume approach for the mass balance equations. Fractures are represented by two-dimensional elements sitting at the interface between 3D matrix cells.

For temporal discretization, the Euler backward method is applied. At each time step, the resulting nonlinear system of discrete equations is solved using the Newton-Raphson method. After obtaining a converged solution, the propagation criterion is assessed to determine if fracture propagation has occurred. If propagation is detected, the entire system is recalculated to account for the updated fracture geometry, and this process continues iteratively until the fracture tip stops advancing. This approach ensures accurate resolution of the evolving fracture geometry and the associated physical properties, ultimately arriving at a stable configuration.

2.3 Fracture propagation

To determine when fracture propagation occurs, an extended virtual crack closure technique (VCCT) (Settgast et al., 2017; Ju et al., 2021) is employed to evaluate the energy release rate (G). The fracture propagates whenever the energy release rate exceeds a critical value (G_c), i.e.

$$G_c = K_{Ic}^2 \frac{1-\nu^2}{E} \tag{12}$$

where K_{Ic} is the fracture toughness (or critical stress intensity factor), ν is the Poisson ratio and E is the Young modulus. Whenever the energy release rate exceeds the critical value ($G > G_c$) the fracture is extended by splitting the nodes adjacent to the face along which the fracture propagates.

There is experimental and observational evidence that the fracture toughness at field scale is higher than what is measured in the laboratory, suggesting a certain scale dependence (Scholz, 2010). To account for this effect, following other works in the literature (see, e.g., (McClure, 2023)) we introduce a toughness scaling factor α, i.e

$$K_{Ic} = K_{Ic,0}(1 + \alpha\sqrt{l_{\text{frac}}}), \tag{13}$$

where $K_{Ic,0}$ is the initial toughness, l_{frac} measures the distance between the fracture edge element and the injection point.

3 Inferred Hydraulic Fracture Shape and Growth Rates from 16A Stage 3 MEQ Data

In this section, we analyze the MEQ data collected during the stimulation of Stage 3 on the 16(A)78-32 well (Dyer et al., 2022) to estimate the fracture shape and its growth rates in both the vertical and horizontal directions.

The spatial distribution of MEQ events suggests that the fracture is fairly circular, indicating that the horizontal and vertical growth rates are similar. To better understand the growth rate of the fracture, Figure 1 presents the distance-time plot for all MEQ events associated with Stage 3. The plot separates the horizontal and vertical distances of each event to identify differences in growth rates between the two directions. The vertical distance envelope exhibits a slightly steeper gradient than the horizontal distance envelope, indicating a marginally faster fracture propagation rate in the vertical direction. Interestingly, this difference is smaller than what would be expected for a smooth stress gradient consistent with the field estimations at Utah FORGE.

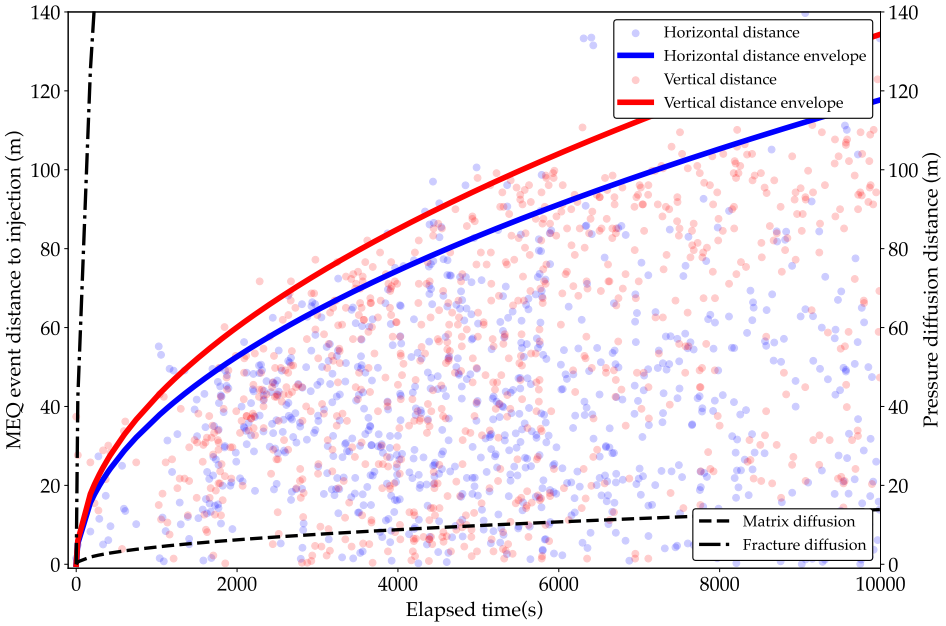

Figure 1: Distance-time plot for MEQ events of Stage 3 in both horizontal and vertical directions.

In the next section, through a numerical study, we investigate whether this behavior could result from an apparent toughness anisotropy induced by stress roughness.

4 Numerical experiments

This section presents a numerical investigation of the Stage 3 hydraulic fracturing stimulation to demonstrate that stress roughness may be the underlying cause of the apparent toughness anisotropy and to further characterize the rock fabric.

To achieve this, hydraulic fracturing simulations of the Stage 3 operation are performed. First, a demonstrative simulation is conducted to validate that far-field fracture growth induced by stress roughness can be effectively reproduced using a model with homogeneous in situ stress and apparent toughness anisotropy.

Following the validation, two versions of the model are run. In the first version, a smooth stress gradient is considered, and the apparent toughness anisotropy is calibrated through history matching with field fracture propagation data inferred from MEQ events. In the second version, the stress profile is extracted from sonic log data to evaluate the expected anisotropy, and the model is rerun incorporating this upscaled stress profile. This approach allows us to compare the calibrated toughness anisotropy with the anisotropy predicted from the stress profile and assess its consistency with observed fracture growth.

Finally, the results are summarized, comparing the calibrated toughness anisotropy parameters to those obtained via a homogenization technique applied to the estimated stress profile. This comparison provides insights into the relationship between stress roughness, toughness anisotropy, and the observed fracture patterns.

4.1 Model setup & parameters

The stimulation of Stage 3 of Well 16A involved the injection of a high viscosity crosslinked gel through a single perforation cluster. To simplify the model and due to some missing components in the modeling tool, several assumptions were introduced:

- The wellbore itself is not included in the simulation.
- The perforation cluster is represented by a single planar fracture. This approach is in line with previous work in the literature (W. Fu et al., 2021).
- Near-wellbore losses, which are expected to be significant given the measured field pressures that would otherwise imply unphysical toughness values, are not explicitly modeled.
- The potential deterioration of the crosslinked gel viscosity after injection is not accounted for in the model.
- No well model is employed and injection is represented by point source with a specified mass flux.
- The presence of proppant is neglected.

Despite these simplifying assumptions, the model effectively serves the purpose of assessing the impact of stress roughness on fracture propagation.

Figure 2 illustrates the problem setup used to model this operation, including the profiles of the initial pressure and minimum horizontal stress. The injection rate, derived from field data, is shown in Figure 3. Key material properties and their respective values for all simulations are summarized in Table 1.

4.2 Case 0: Validation example

We begin with a validation example to test whether our specific model setup, which includes leakoff effects, the Stage 3 geometry, and the corresponding injection rate, can replicate the

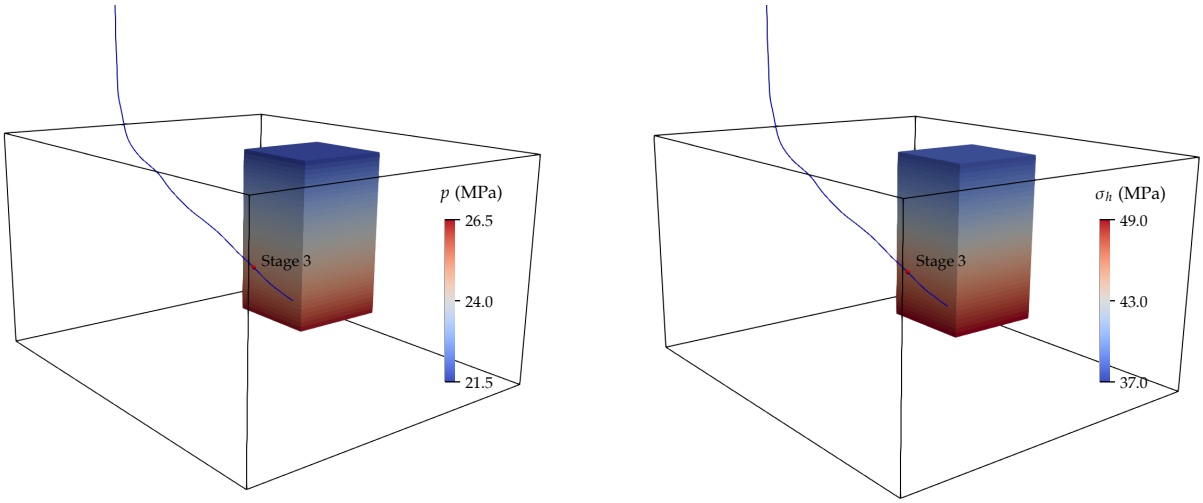

Figure 2: Problem setup for the hydraulic fracturing simulation for Stage 3.

observed fracture geometry using toughness anisotropy. Specifically, we aim to demonstrate that a model incorporating apparent toughness anisotropy can reproduce the fracture geometry induced by a corresponding stress roughness pattern.

For validation purposes, we design a stress roughness profile using a periodic function, following the approach of P. Fu et al. (2019) and Dontsov and Suarez-Rivera (2021):

$$\sigma_h(z) = \sigma_{h0}(z) + \Delta\sigma_h f(z), \tag{14}$$

where

$$f(z) = \sum_{n=-\infty}^{\infty} \left[H(z - 2nh)H((2n+1)h - z) - H(z - (2n+1)h)H((2n+2)h - z) \right], \tag{15}$$

and $H(\cdot)$ represents the Heaviside function. Here, $\sigma_{h0}(z)$ denotes the homogeneous stress profile consistent with the gravitational load and the specified rock properties, as shown in Figure 2. For this example, we select $\Delta\sigma_h = 0.5$ MPa and $h = 10$ m. According to the relationships developed in P. Fu et al. (2019) and Dontsov and Suarez-Rivera (2021), these parameters result in a differential toughness given by

$$\Delta K_{Ic} := K_{Ic,v} - K_{Ic,h} \approx 1.6\,\text{MPa} \cdot \sqrt{\text{m}}. \tag{16}$$

Figures 4 and 5 compare the simulation results for the periodic stress roughness case and the corresponding apparent toughness anisotropy case. The results demonstrate close agreement between the two scenarios in terms of aperture magnitude and fracture geometry at $t \approx 30$

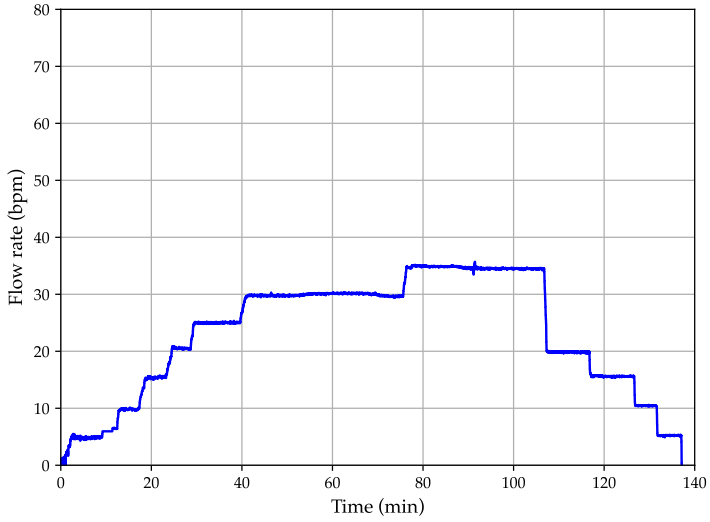

h

Figure 3: Stage 3 injection rate used in the hydraulic fracturing simulation.

Rock matrix	**Values**	**Units**
Young's modulus, E	27.58	GPa
Poisson's ratio, ν	0.3	-
Permeability, k	50×10^{-18}	m^2
Initial porosity, ϕ_0	0.01	-
Compressibility of porosity, c_ϕ	10^{-10}	Pa^{-1}
Rock fracture		
Horizontal rock toughness, $K_{Ic,h}$	5.0	MPa·$\sqrt{m}$
Vertical rock toughness, $K_{Ic,v}$	$K_{Ic,h} + \Delta K_{Ic}$	MPa·$\sqrt{m}$
Initial aperture, ω_0	0.04	mm
Matrix fluid (water)		
Viscosity, μ_f	0.001	Pa·s
Compressibility, c_w	5×10^{-10}	Pa^{-1}
Fracture fluid (gel)		
Viscosity, μ_f	0.070	Pa·s
Compressibility, c_g	5×10^{-10}	Pa^{-1}

Table 1: Material properties adopted in the hydraulic fracturing simulation.

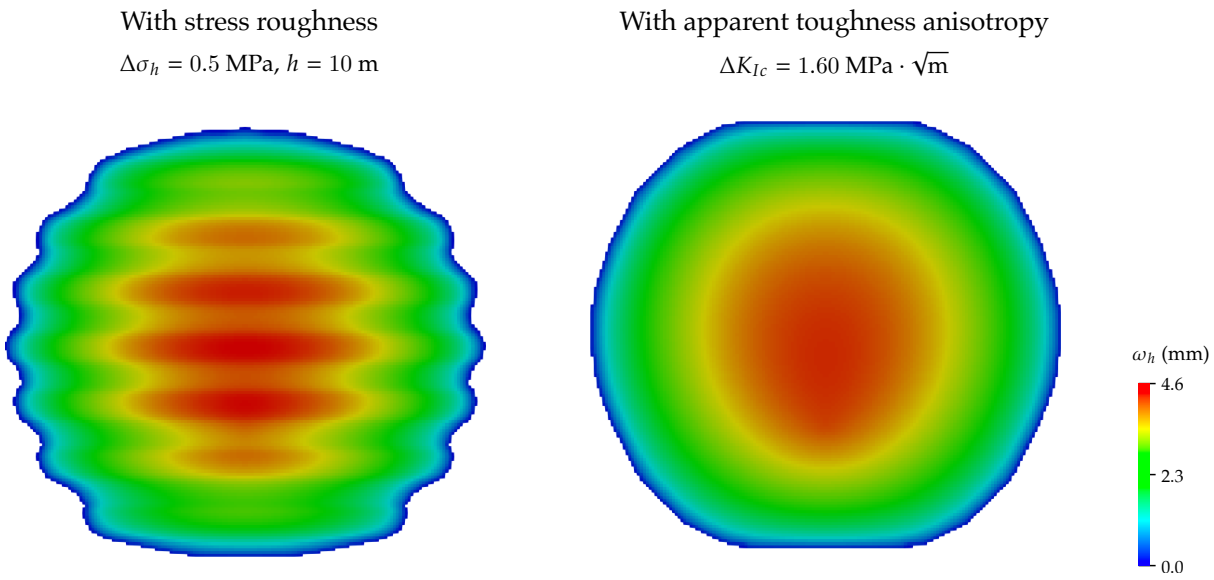

Figure 4: Comparison in fracture aperture at $t \approx 30$ minutes of injection between the case with periodic stress roughness and the case with corresponding apparent toughness anisotropy.

minutes. Moreover, Figure 5b illustrates that the fracture size evolution is nearly identical in both horizontal and vertical directions.

Based on these results, we conclude that our hydraulic fracturing model, when incorporating specific apparent toughness anisotropy, can equivalently reproduce the far-field fracture geometry induced by a rough stress profile. This validation supports the notion that stress roughness features can be effectively characterized through parameter calibration of apparent toughness anisotropy using our hydraulic fracturing solver.

4.3 Case 1: Calibration of apparent toughness anisotropy

Let us now calibrate the apparent toughness anisotropy to infer the possible characteristics of in situ stress. It is important to note that this calibration is performed manually rather than using an automated history-matching tool, so the resulting parameters may not represent the optimal solution.

Figure 6a shows the fracture growth over time, comparing the simulation results using calibrated parameters $\Delta K_{Ic} = 0.5$ MPa$\cdot\sqrt{\text{m}}$ and $\alpha = 0.55$ m$^{-1/2}$ with those inferred from MEQ data. The modeled fracture propagation closely matches the field observations in both horizontal and vertical directions. With the adopted stress gradient and toughness anisotropy, the simulation also captures the discrepancy between horizontal and vertical growth.

To further highlight the effects of toughness anisotropy, we repeat the simulation with

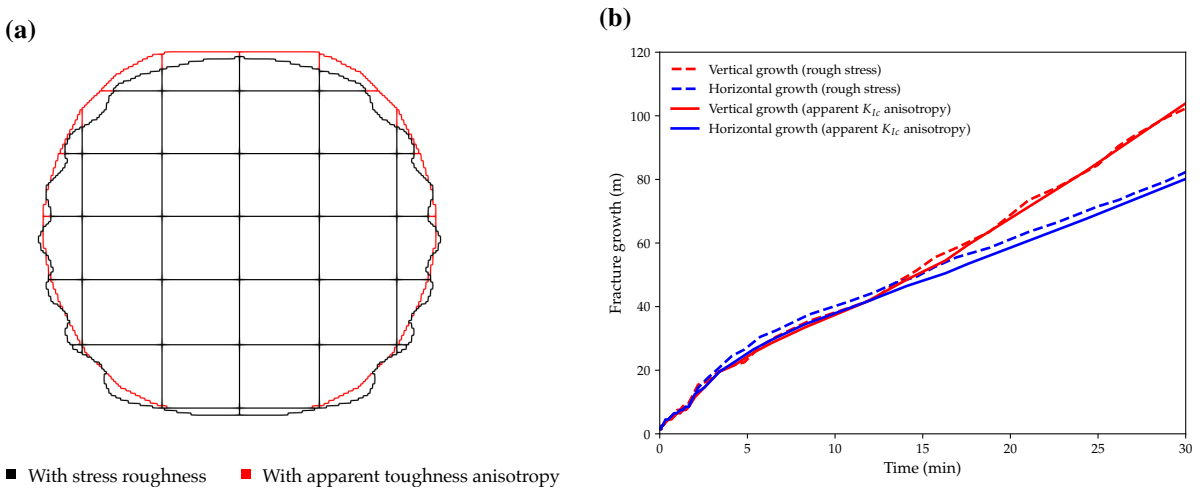

Figure 5: Comparison in simulation results between the case with periodic stress roughness and the case with corresponding apparent toughness anisotropy: (a) fracture geometry at $t \approx 30$ minutes, (b) fracture geometry evolution in both horizontal and vertical directions.

isotropic rock toughness (*i.e.,* $K_{Ic,v} = K_{Ic,h}$), keeping all other parameters unchanged. Figure 6b presents the results for the isotropic case compared to the fracture growth inferred from MEQ data. While the horizontal growth remains consistent with the field results, the vertical growth in the isotropic case is excessively rapid, confirming that a certain degree of toughness anisotropy is necessary to match field observations.

Notably, the simulated fracture propagation for both cases nearly ceases after $t = 120$ minutes. This behavior is expected, as the injection rate gradually reduces to zero after this point, halting further fracture propagation in the simulation. However, field results inferred from MEQ data suggest continued fracture growth even after injection stops. A possible explanation is that microseismic events might occur with a delay relative to the actual fracture propagation, leading to an underestimation of fracture growth when inferred solely from MEQ data. For the purposes of this study, we continue to use the MEQ data to infer fracture growth while acknowledging its potential limitations.

Figure 7 shows the simulation results with the calibrated parameters at the end of the simulation ($t = 160$ minutes). The fracture exhibits a nearly circular shape, with a size comparable to the range of observed microseismic events. The fracture aperture reaches over 20 mm at the end of the injection period. This large aperture is likely due to limited leak-off in the model, a result of the high-viscosity fluid in the fracture and the low matrix permeability provided in Table 1 (see Remark 2 for further discussion on potential effects of leak-off on modeling results).

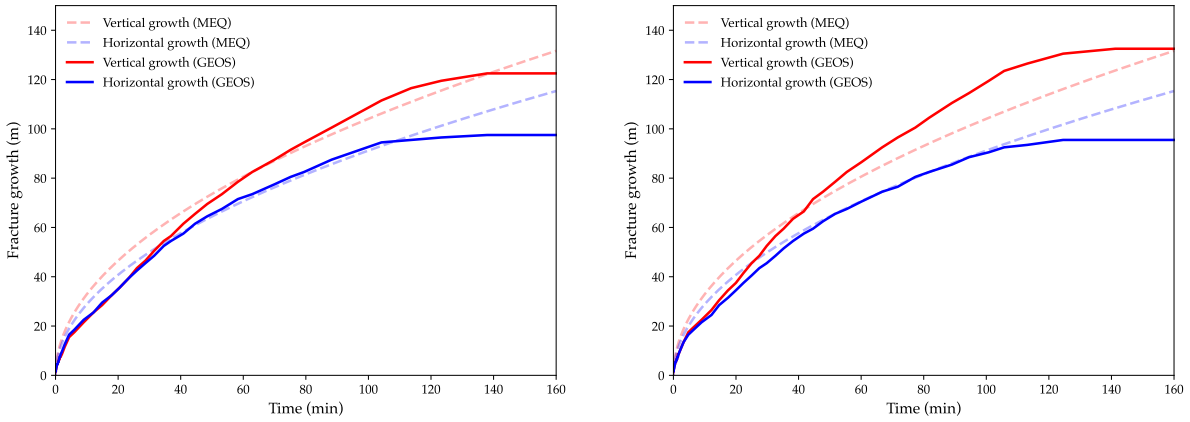

Figure 6: Comparison in fracture geometry evolution inferred from MEQ data and that from hydraulic simulation results with (a) calibrated toughness anisotropy, and (b) isotropic toughness.

Additionally, the hydraulic fracture demonstrates an upward growth tendency, as indicated by the contours of rupture/fracturing time. This behavior is expected because the stress gradient typically exceeds the pore pressure gradient, as shown in Figure 2, making upward fracture propagation more favorable than downward growth.

Remark 1. Note that the initial aperture ($\omega_0 = 0.04$ mm) is significantly smaller than the average aperture (≈ 12 mm) obtained in the simulation. Therefore, the error in the global mass balance caused by the mass creation from new fracture elements is assumed to be negligible.

Remark 2. The leak-off in the current model may be underestimated due to the high viscosity of the fracking gel and the low matrix permeability adopted, both of which are based on Utah FORGE references (Ghassemi & Zhou, 2022; Xing et al., 2023). In reality, matrix permeability could increase during fracture propagation as a result of microcrack formation or damage generation around the fracture plane. Furthermore, the viscosity of the fracking gel may decrease over time and with increasing temperature. For simplicity, both matrix permeability and gel viscosity are treated as constant in the current model. This simplification likely underestimates the actual leak-off, leading to excessively large fracture apertures and/or overestimated fracture sizes in the simulations. This also explains the need for a toughness scaling factor to constrain fracture growth. In future work, we plan to incorporate a variable matrix permeability to better account for the potential for increased leak-off and its impact on fracture behavior.

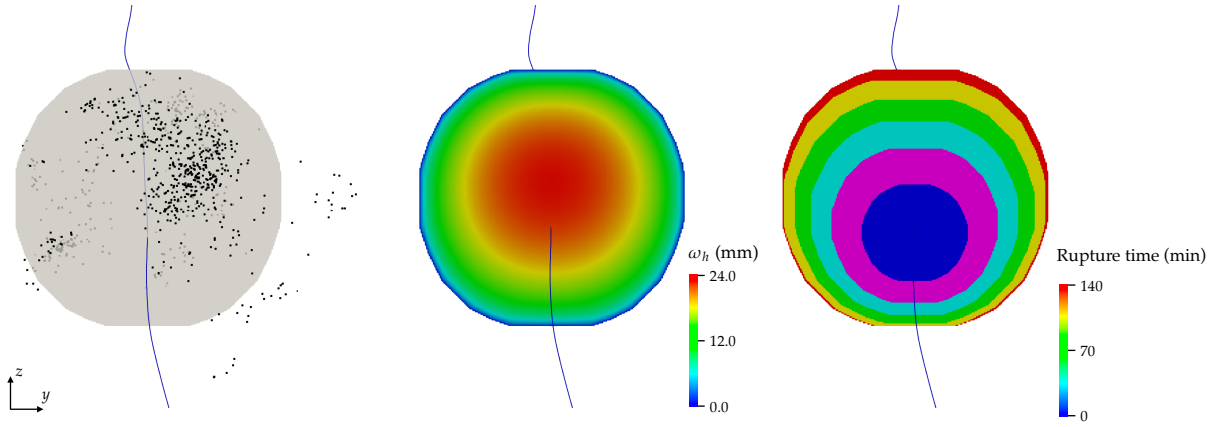

Figure 7: Simulation results with the calibrated ΔK_{Ic} at $t = 160$ minutes. The left panel depicts the modeled fracture geometry alongside the MEQ events. The middle panel shows the final fracture aperture, and the right panel illustrates the fracturing time.

4.4 Case 2: Isotropic toughness with rough stress profile

Let us now consider the same setup by explicitly incorporating the in situ stress profile inferred from the sonic log collected along Well 16B (May & Jones, 2023), while keeping the toughness isotropic. The choice of using the sonic log from Well 16B was dictated by the unavailability of logs for Well 16A at the depth of the Stage 3 injection. The measured minimum horizontal stress profile is shown as the gray line in Figure 8a. However, the resolution of this stress profile is too fine for use in our numerical simulations. To address this, we upscale, the stress distribution to mesh with a vertical resolution of 2 m, by averaging the stress values within each grid cell to preserve the total force applied to each cell. The upscaled stress profile is shown as the solid black line in Figure 8a. Figure 8b illustrates the resulting stress distribution over the interval TVD $\in [2325, 2535]$ m, with the location of Stage 3 marked on the figure.

Figures 9 and 10 present the simulation results for the case with the field in situ stress profile. Notably, the fracture geometry closely resembles the spatial distribution of microseismic (MEQ) events without requiring parameter calibration. The fracture is not perfectly circular but instead takes on a rounded pentagonal shape, as depicted in Figure 10. This shape is consistent with the MEQ distribution pattern, where the lower part of the fracture is wider than the upper part, closely mirroring the rounded pentagonal geometry observed in the field. It is also remarkable that the modeled fracture geometry aligns reasonably well with the MEQ data, despite using the stress profile measured at Well 16B rather than Well 16A, where the injection actually occurred. However, there are differences in propagation speed between the simulation and MEQ data. The modeled fracture growth in both horizontal and vertical directions is generally faster than that inferred from MEQ data. This discrepancy may reflect an actual difference in field behavior, but

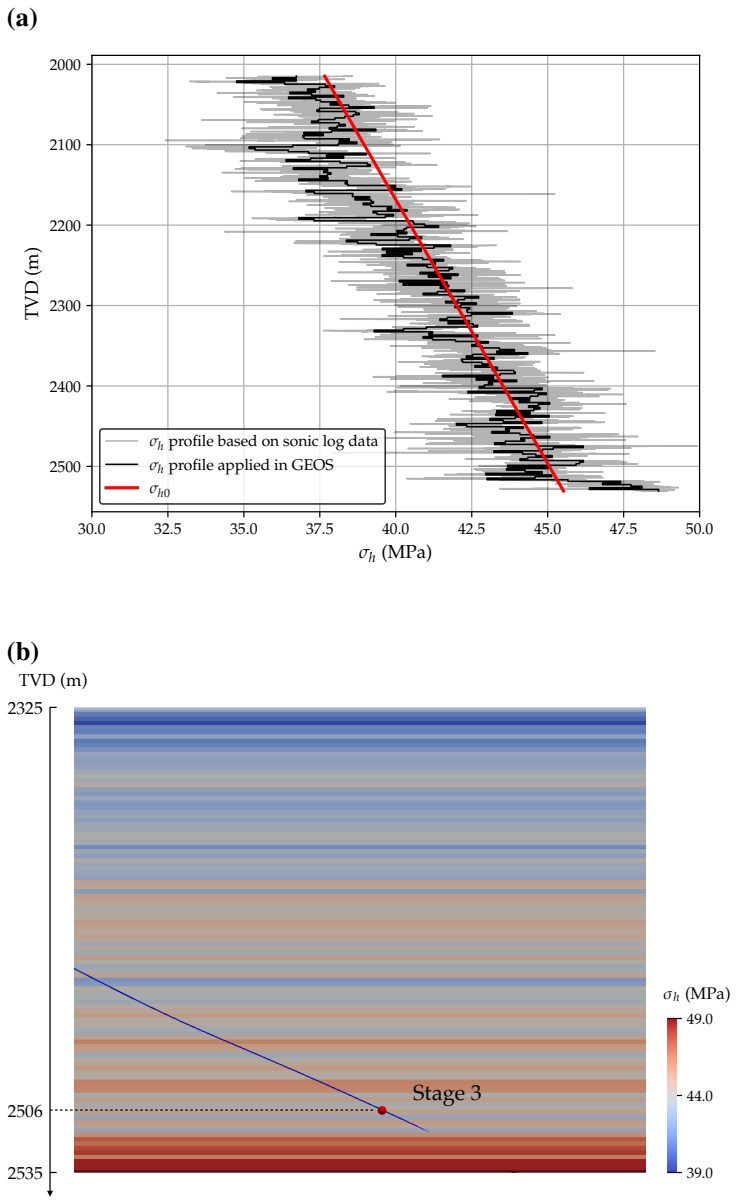

Figure 8: Stress profile of σ_h: (a) plots of the original stress profile based on the sonic log data (gray), the upscaled version applied in the model (black), and the homogeneous stress profile (red), (b) the resulting distribution of σ_h over the interval TVD $\in [2325, 2535]$ m.

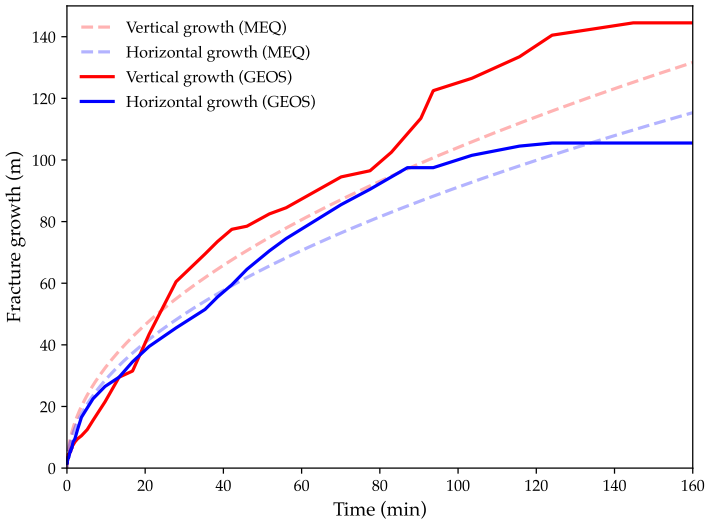

Figure 9: Comparison in fracture geometry evolution inferred from MEQ data and that from hydraulic simulation results with the field stress profile.

it could also arise from the limitations of MEQ-based estimations, which may underestimate fracture growth due to delays in detecting microseismic events relative to actual propagation.

Remark that the fracture aperture, the average magnitude is comparable to that obtained with calibrated toughness anisotropy. The maximum aperture is slightly larger, likely because the fracture has crossed a layer with lower stress. The contour of rupture/fracturing time still indicates that the fracture tends to grow upwards, driven by the stress gradient.

4.5 Comparison of calibrated and inferred apparent toughness anisotropy

Let us now compare the calibrated apparent toughness anisotropy presented in Section 4.3 with the anisotropy that one would expect given the stress profile measure from the image logs. To this end, we apply the homogenization method proposed by Dontsov and Suarez-Rivera (2021) to estimate an "analytical" apparent toughness anisotropy based on the field stress profile shown by the gray line in Figure 8,

$$\Delta K_{Ic} = \sqrt{\frac{2}{\pi}} \int_0^\infty \frac{\sigma_h(s) - \sigma_{h0}(s)}{\sqrt{s}} \, \mathrm{d}s, \tag{17}$$

where s is a local coordinate originating at the fracture tip and increasing toward the fracture interior.

Here, the origin of s is defined at the fracture tip at $t = 160$ minutes, located approximately 131 m above the injection point. Also, since the stress profile is available only up to a total

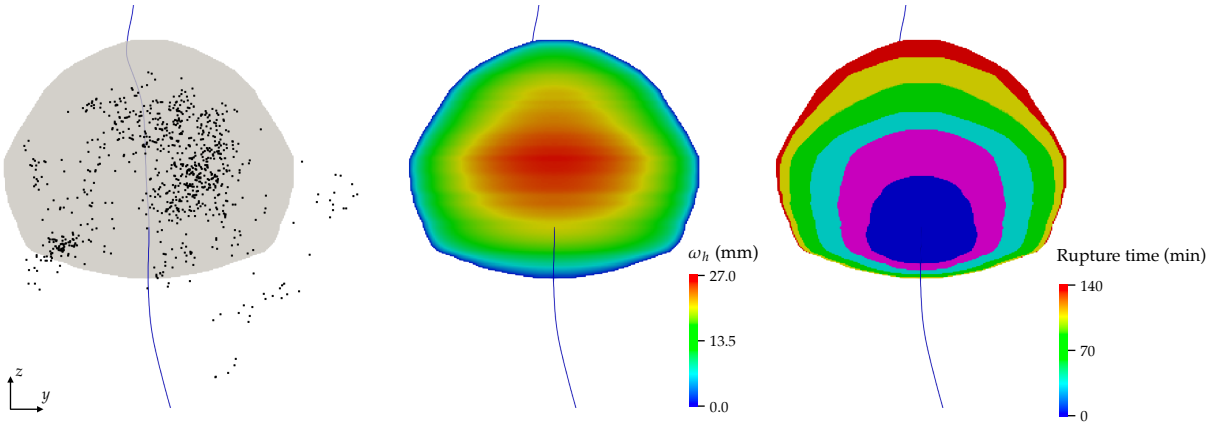

Figure 10: Simulation results with the field stress profile at $t = 160$ minutes. The left panel depicts the modeled fracture geometry alongside the MEQ events. The middle panel shows the final fracture aperture, and the right panel illustrates the fracturing time.

vertical depth (TVD) of 2530 m, the integration cannot extend to infinity. Despite this, we can still estimate ΔK_{Ic} and the resulting ΔK_{Ic} is approximately $0.27\,\text{MPa} \cdot \sqrt{\text{m}}$, which is comparable to the calibrated value of $0.55\,\text{MPa} \cdot \sqrt{\text{m}}$. This overall agreement suggests that the calibrated toughness anisotropy may indeed be the effect of a nonsmooth stress profile of which additional evidence is present in the sonic logs.

According to P. Fu et al. (2019), the apparent toughness anisotropy is positively correlated with the magnitude of stress variation and a characteristic length that defines the wavelength of the roughness. This characteristic length is also closely associated with the rock fabric features. Notably, the toughness anisotropy obtained from both the hydraulic fracturing simulation and the analytical homogenization technique exhibits a relatively small magnitude. This observation suggests that either the stress roughness magnitude or the characteristic length (or both) are relatively small. Based on the stress profile shown in Figure 8a, the stress variation can be roughly estimated at 2 MPa, which corresponds to a characteristic length of approximately $10 - 70$ mm for the rock fabric.

5 Conclusions & Future work

This report presents a numerical investigation of the Stage 3 stimulation on the 16(A)78-32 Well at the Utah FORGE site, focusing on characterizing the in situ stress roughness and rock fabric features. To do so, we have built upon previous studies (P. Fu et al., 2019; Dontsov & Suarez-Rivera, 2021), which established a relationship between stress roughness and apparent toughness anisotropy, and conducted hydraulic fracturing simulations that incorporate both

anisotropic rock toughness . With the well calibrated toughness anisotropy, the model can reasonably reproduce the fracture growth in both vertical and horizontal directions, as inferred from the MEQ data. Additionally, a simulation incorporating the stress profile derived from field sonic log data has been performed, producing a fracture geometry consistent with the microseismic cloud, thereby suggesting that the rough stress profile may indeed be the source of the apparent toughness anisotropy in the field. Finally, to further confirm this hypothesis, the stress profile extracted from the sonic log collected a Well 16B was then used to analytically compute the toughness anisotropy in the field. This value was then compared to the calibrated toughness anisotropy.

Future work will focus on applying this numerical workflow to other stimulation stages on both the injection (16(A)78-32) and production (16(B)78-32) wells. The new simulation results will serve to further validate and strengthen the observations and conclusions presented in this report.

Data availability

All numerical simulations were performed using the open-source GEOS simulation framework (Settgast et al., 2024) and simulation decks are available at https://github.com/GEOS-DEV/FORGE.

References

Dontsov, E., & Suarez-Rivera, R. (2021). Representation of high resolution rock properties on a coarser grid for hydraulic fracture modeling. *Journal of Petroleum Science and Engineering*, *198*, 108144.

Dyer, B., Karvounis, D., & Bethmann, F. (2022, 11). *Utah forge: Updated seismic event catalogue from the april, 2022 stimulation of well 16a(78)-32.* Retrieved from `https://gdr.openei.org/submissions/1429` doi: 10.15121/1908927

Fu, P., Huang, J., Settgast, R. R., Morris, J. P., & Ryerson, F. J. (2019). Apparent toughness anisotropy induced by "roughness" of in-situ stress: a mechanism that hinders vertical growth of hydraulic fractures and its simplified modeling. *SPE Journal*, *24*(05), 2148–2162.

Fu, W., Morris, J. P., Fu, P., Huang, J., Sherman, C. S., Settgast, R. R., & Ryerson, F. J. (2021). Developing upscaling approach for swarming hydraulic fractures observed at hydraulic fracturing test site through multiscale simulations. *SPE Journal*, *26*(05), 2670–2684.

Ghassemi, A., & Zhou, X. J. (2022, 10). *Utah forge 5-2615: Well 58-32 and 78-32 poroelastic properties.* Retrieved from https://gdr.openei.org/submissions/1464 doi: 10.15121/1999253

Ju, X., Fu, P., Settegast, R. R., & Morris, J. P. (2021). A coupled thermo-hydro-mechanical model for simulating leakoff-dominated hydraulic fracturing with application to geologic carbon storage. *International Journal of Greenhouse Gas Control*, *109*, 103379. Retrieved from https://www.sciencedirect.com/science/article/pii/S1750583621001316 doi: https://doi.org/10.1016/j.ijggc.2021.103379

May, D., & Jones, D. (2023, 09). *Utah forge: Well 16b(78)-32 logs from schlumberger technologies.* Retrieved from https://gdr.openei.org/submissions/1531 doi: 10.15121/2001059

McClure, M. (2023). Calibration parameters required to match the utah forge 16a (78)-32 stage 3 stimulation with a planar fracturing model. In *Proceedings, 48th workshop on geothermal reservoir engineering stanford university, stanford, california, february 6-8, 2023 sgp -tr-224.*

Scholz, C. H. (2010). A note on the scaling relations for opening mode fractures in rock. *Journal of Structural Geology*, *32*(10), 1485-1487. Retrieved from https://www.sciencedirect.com/science/article/pii/S019181411000163X doi: https://doi.org/10.1016/j.jsg.2010.09.007

Settgast, R. R., Aronson, R. M., Besset, J. R., Borio, A., Bui, Q. M., Byer, T. J., ... Wu, H. (2024). Geos: A performance portable multi-physics simulation framework for subsurface applications. *Journal of Open Source Software*, *9*(102), 6973. Retrieved from https://doi.org/10.21105/joss.06973 doi: 10.21105/joss.06973

Settgast, R. R., Fu, P., Walsh, S. D., White, J. A., Annavarapu, C., & Ryerson, F. J. (2017). A fully coupled method for massively parallel simulation of hydraulically driven fractures in 3-dimensions. *International Journal for Numerical and Analytical Methods in Geomechanics*, *41*(5), 627-653. Retrieved from https://onlinelibrary.wiley.com/doi/abs/10.1002/nag.2557 doi: https://doi.org/10.1002/nag.2557

Xing, P., Damjanac, B., Radakovic-Guzina, Z., Torres, M., Finnila, A., Podgorney, R., ... McLennan, J. (2023). Comparison of modeling results with data recorded during field stimulations at utah forge site. In *48th workshop on geothermal reservoir engineering, stanford, ca.*

Zoback, M., Ruths, T., McClure, M., Singh, A., Kohli, A., Hall, B., ... Kintzing, M. (2022). Lithologically-controlled variations of the least principal stress with depth and resultant <italic>frac fingerprints</italic> during multi-stage hydraulic fracturing. In *Unconventional*

resources technology conference, 20–22 june 2022 (p. 420-436). Retrieved from https://library.seg.org/doi/abs/10.15530/urtec-2022-3722883 doi: 10.15530/urtec-2022-3722883